Generation and Conversion Dynamics of Dual Bessel Beams with a Photonic Spin-Dependent Dielectric Metasurface

Tianyue Li[,1] Xingyi Li,[2,3] Shaohui Yan[,2,3] Xiaohao Xu[,4] Shuming Wang[,1,5,*] Baoli Yao[,2,3] Zhenlin Wang,[1] and Shining Zhu[1,5]

[1]*National Laboratory of Solid-State Microstructures, School of Physics, College of Engineering and Applied Sciences, Nanjing University, Nanjing 210093, China*

[2]*State Key Laboratory of Transient Optics and Photonics Xi'an Institute of Optics and Precision Mechanics (XIOPM), Chinese Academy of Sciences (CAS), Xi'an 710119, China*

[3]*University of Chinese Academy of Sciences, Beijing 100049, China*

[4]*Guangdong Provincial Key Laboratory of Optical Fiber Sensing and Communications, Institute of Nanophotonics, Jinan University, Guangzhou 511443, China*

[5]*Key Laboratory of Intelligent Optical Sensing and Manipulation Ministry of Education, Nanjing 210093, China*

A Bessel beam has the properties of propagation invariance and a self-healing effect, leading to a variety of interesting phenomena and applications. Recently, as a planar diffractive element with miniaturized size, metasurfaces are widely employed to manipulate light in the subwavelength region, including generating a Bessel beam. However, such a metasurface-generated Bessel beam allows output light with no tunable functions. Here, with the interplay of the geometric phase and the dynamic phase, we propose a method to generate and allow conversion from any orthogonal polarizations to independent Bessel beams with a single-layer dielectric metasurface. The simulation results indicate that the arbitrary conversion between different Bessel beams is related to the spin-dependent orbit motion caused by the tight-focusing effect, leading to the singularity of the spot. This physical mechanism is well studied and the theoretical model for revealing the dependence of different incident polarization on the conversion dynamics is presented. Our approach paves a way for efficient generation and multifunctional applications, ranging from high-numerical-aperture devices to compact nanophotonic platforms for spin-dependent structured beams.

I. INTRODUCTION

Bessel beams, as the most familiar type of nondiffracting beams, have many intriguing properties and have been extensively studied since first being introduction in 1987 by Durnin [1]. Considerable phenomena and applications related to Bessel beams have been previously reported, such as the artificial Einstein's ring [2], light-sheet microscopy [3,4], superresolution imaging [5], and optical trapping [6,7]. However, conventional techniques for generating Bessel beams involve annular slits [8], an axicon [9], and computer-generated holograms [10,11] based on a traditional optical system with intrinsic limits. For an axicon, the full width at half minimum (FWHM) is restricted and the designed lens usually has a low numerical aperture (NA) due to total internal reflection and fabrication limits. Other methods are faced with a variety of bulky devices and complex systems [12].

To overcome the aforementioned limits, highly integrated planar diffractive elements (PDEs), with the promising development of miniature devices, are used to generate such structured light beams [13]. One example of a promising PDE is the subwavelength metasurface [14], which is primarily dependent on either the geometric phase [15,16] (i.e., Pancharatnam-Berry phase) or the dynamic phase [17], corresponding to the rotation of the orientation angle relative to the reference axis of meta-atoms and the design of a special structure, nanofins. Metasurfaces possess the ability to allow subwavelength focusing into an Airy spot, with a size of $0.61\lambda/\text{NA}$, to reach the Rayleigh diffraction limit, and thus, realize high-resolution imaging [18–22] and a multiphoton quantum source [23]. Furthermore, improving image resolution by breaking the diffraction limit for superresolution microscopy and precise optical manipulation have become subjects of great interest. Recent studies have shown that the zeroth-order Bessel beam generated by PDEs has a main lobe with a size of $0.38\lambda/\text{NA}$, reaching the subdiffraction limit, which could be extended into a needlelike region for light-sheet

———————
*wangshuming@nju.edu.cn

scanning. Additionally, the superposition of Bessel beams with orders of $n = \pm 1$ can be used as a tractor beam for pulling small objects against the propagation direction of light [13,24–26]. Although the generation of a Bessel beam via a metasurface has been reported [12,27,28], the highly purified Bessel beam is usually generated by the arrangement of optimized meta-atoms based on the geometric phase only, and the generation of an arbitrary Bessel beam with independent properties based on a single-layer device has not been reported. On the other hand, the investigation of a Bessel beam with a high NA is associated with the tight-focusing effect, which involves the spin-orbit interaction [29,30]. Previous work has demonstrated a conversion of left- and right-circular polarization, eigen states of spin angular momentum (SAM), into states with arbitrary values of OAM by means of a J-plate [31]. The output light there is actually in paraxial regime, excluding the influence of longitudinal component of the light field and hence isolating us from a rich variety of advanced applications involving tight focusing [30,32,33].

Herein, we propose a compact all-dielectric metasurface to generate and allow the conversion from an arbitrary spin state to absolutely independent Bessel beams. Previous studies have revealed that the modulated phase exhibits the spin-dependent characteristic by combining the geometric phase and the dynamic phase [28,34–37]. For proof-of-concept purposes, we design and numerically demonstrate the generation and conversion of Bessel beams with independent orders and different NAs. Additionally, the symmetric and asymmetric splitting of dual-Bessel beams

is also realized based on the method. The singularity of the spot during the conversion process caused by the tight-focusing effect with a high NA is studied, and the theoretical model of light-field estimation is presented. Our approach may have potential applications in multifunctional nanophotonic platforms, such as compact optical microscopy and switchable optical tweezers, where Bessel beams are required.

II. DESIGN PRINCIPLE

Figure 1(a) depicts a schematic diagram of the photonic spin-dependent dual-Bessel beam generator, where α denotes the aperture angle, the sine of which gives the numerical aperture: $\text{NA} = \sin(\alpha)$. To allow the metasurface device to have different optical responses for orthogonal spin states normally incident on the metasurface, it is necessary to simultaneously satisfy the following conditions:

$$J(x,y)|k^-\rangle = e^{i\varphi^+(x,y)}|(k^-)^*\rangle,$$

$$J(x,y)|k^+\rangle = e^{i\varphi^-(x,y)}|(k^+)^*\rangle, \quad (1)$$

where $J(x,y)$ represents the Jones matrix; $|k^+\rangle$ and $|k^-\rangle$ represent two arbitrary orthogonal spin states, with $\varphi^+(x,y)$ and $\varphi^-(x,y)$ being the corresponding uncorrelated phase profiles; and * denotes the complex conjugate. Since the two photonic spin states in the quantum optics
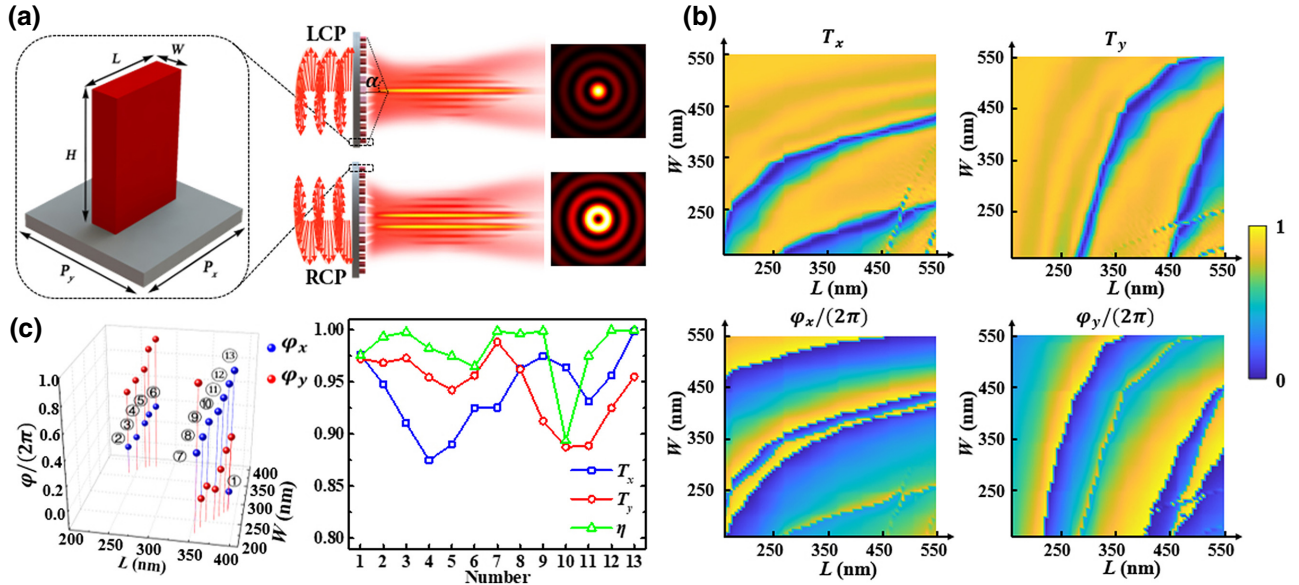

FIG. 1. (a) Schematic diagram of spin-dependent Bessel beam generator formed by Si nanofins with length L, height H, and width W. P_x and P_y indicate the periods of the structure along the x and y directions, respectively. Right insets show Bessel beams with independent orders and opposite circular polarization. (b) Transmittances (T_x and T_y) and phase shifts (φ_x and φ_y) as a function of the nanofin size parameters, L and W. (c) Phase shifts of 13 labeled nanofins, together with corresponding transmittances and polarization conversion efficiencies of the selected nanofins.

correspond to the orthogonal circular polarization (CP) states with the electric and magnetic fields rotating about the wave vector direction in the wave optics [29], the orthogonal CP states are chosen to be the spin states by the forms $|k^-\rangle = |L\rangle = \frac{1}{\sqrt{2}}\begin{bmatrix} 1 \\ i \end{bmatrix}$ and $|k^+\rangle = |R\rangle = \frac{1}{\sqrt{2}}\begin{bmatrix} 1 \\ -i \end{bmatrix}$, where $|L\rangle$ and $|R\rangle$ denote left-handed circular polarized (LCP) and right-handed circular polarized (RCP) states, respectively. Therefore, the Jones matrix $J(x,y)$ can subsequently become

$$J(x,y) = \frac{1}{2}\begin{bmatrix} e^{i\varphi^+(x,y)} & e^{i\varphi^-(x,y)} \\ -ie^{i\varphi^+(x,y)} & -ie^{i\varphi^-(x,y)} \end{bmatrix}\begin{bmatrix} 1 & 1 \\ i & -i \end{bmatrix}^{-1}. \quad (2)$$

The eigenvalues and eigenvectors of the Jones matrix can be obtained by solving Eq. (2), so the relationship between the phase profiles of the LCP and RCP states and the phase shifts of nanofins along two perpendicular symmetry axes can be expressed as follows:

$$|\varphi_x - \varphi_y| = \pi,$$

$$\varphi^+(x,y) = \varphi_x + 2\theta,$$

$$\varphi^-(x,y) = \varphi_x - 2\theta. \quad (3)$$

According to Eq. (3), one needs to build a phase library of nanofins to realize the specific phase difference between the dynamic phase φ_x and φ_y by changing the geometry of the nanofin and material refractive index, and the geometric phase is controlled only by rotation of the orientation angle θ. By the combination of the dynamic phase and the geometric phase, when the beam passes through the nanofin, the LCP and RCP states can be transformed into their orthogonal polarization states and possess the same dynamic phase and opposite geometric phase, to realize uncorrelated phase control.

Based on the above discussion, the specially designed unit cell, composed of silicon (Si) on a fused silica (SiO$_2$) substrate, is shown in the left inset of Fig. 1(a), which can be considered as a birefringent waveguide [17,35] because of the high-index contrast between the nanofin ($n_{Si} = 3.48$) and air ($n_{air} = 1$). Finite-difference time domain simulations are performed to calculate transmittance, while periodic boundary conditions are applied along x and y axes, and the perfectly matched layers (PMLs) are applied to the z direction. The working wavelength is set as $\lambda = 1550$ nm, the heights of the selected nanofins are fixed at $H = 1500$ nm, and the properly arranged array of nanofins have a lattice constant of $P_x = P_y = 600$ nm. The range of lengths (L) and widths (W) of the nanofins covers 200 to 550 nm, for 5 nm increments of each geometric variable, and the results of transmittance T_x and T_y and phase shifts φ_x and φ_y along the x and y axes are shown in the

right inset of Fig. 1(b). The phase library is built based on 13 nanofins, which provide 13 phase shifts, high transmittances, and polarization conversion efficiencies, as shown in Fig. 1(c).

III. BESSEL BEAM WITH INDEPENDENT ORDERS

The scalar form of Bessel beams propagating along the z axis, in cylindrical coordinates (r, ϕ, z), can be described by

$$E(r,\phi,z) = AJ_n(k_r r)exp(ik_z z)exp(\pm in\phi), \quad (4)$$

where A is the amplitude; J_n is the nth Bessel function of the first kind; $k = 2\pi/\lambda$ is the total wave number; k_z and k_r are the longitudinal and transverse wave numbers, respectively, that follow the relation $\sqrt{k_z^2 + k_r^2} = k$; and $\phi = \arctan(y/x)$ is the azimuthal angle, which represents the higher-order Bessel beam imparted by the optical vortex.

For comparison with the optimized geometric-phase-based metasurface, the target phase profile of the spin-dependent Bessel beam can be written as follows [12]:

$$\varphi^+(x,y) = -\frac{2\pi}{\lambda}\sqrt{x^2 + y^2}NA_1 + n\phi$$

$$\varphi^-(x,y) = -\frac{2\pi}{\lambda}\sqrt{x^2 + y^2}NA_2 + (n+1)\phi \quad (5)$$

where (x, y) represents the position of each nanofin, λ is the working wavelength in free space, and NA is the numerical aperture of the metasurface. Here, we keep the parameter $NA_1 = NA_2 = 0.4$ and demonstrate the orders $n_1 = 0$ and $n_2 = 1$ for case 1, and $n_1' = 2$ and $n_2' = 3$ for case 2, using two samples with $R = 12$ μm. The longitudinal intensity distributions; calculated [using Eq. (4)] and simulated transverse intensity distributions with FWHM$_1 \sim 0.855$ μm, FWHM$_2 \sim 0.758$ μm, FWHM$_1' \sim 0.860$ μm, and FWHM$_2' \sim 0.825$ μm; and the corresponding Stokes parameter S_3, indicating the interpretation of the difference in relative intensity of orthogonal CP states, are shown in Figs. 2(a)–2(d). The calculated efficiencies (defined as the ratio of the power of the spot in the x-y plane to incident power) for LCP and RCP incidences are 61.53% and 61.40% for case 1 and 60.02% and 57.84% for case 2.

To observe and analyze the continuous conversion of Bessel beams of different orders, CP states with different polarization angles are normally illuminated only. Therefore, the conversion dynamics of the transverse pattern with polarization angles, δ, from $-\pi/2$ to $\pi/2$ can be shown on the hybrid-order Poincaré sphere (PS) [38], as shown in Figs. 2(e) and 2(f). It can be seen that the spots
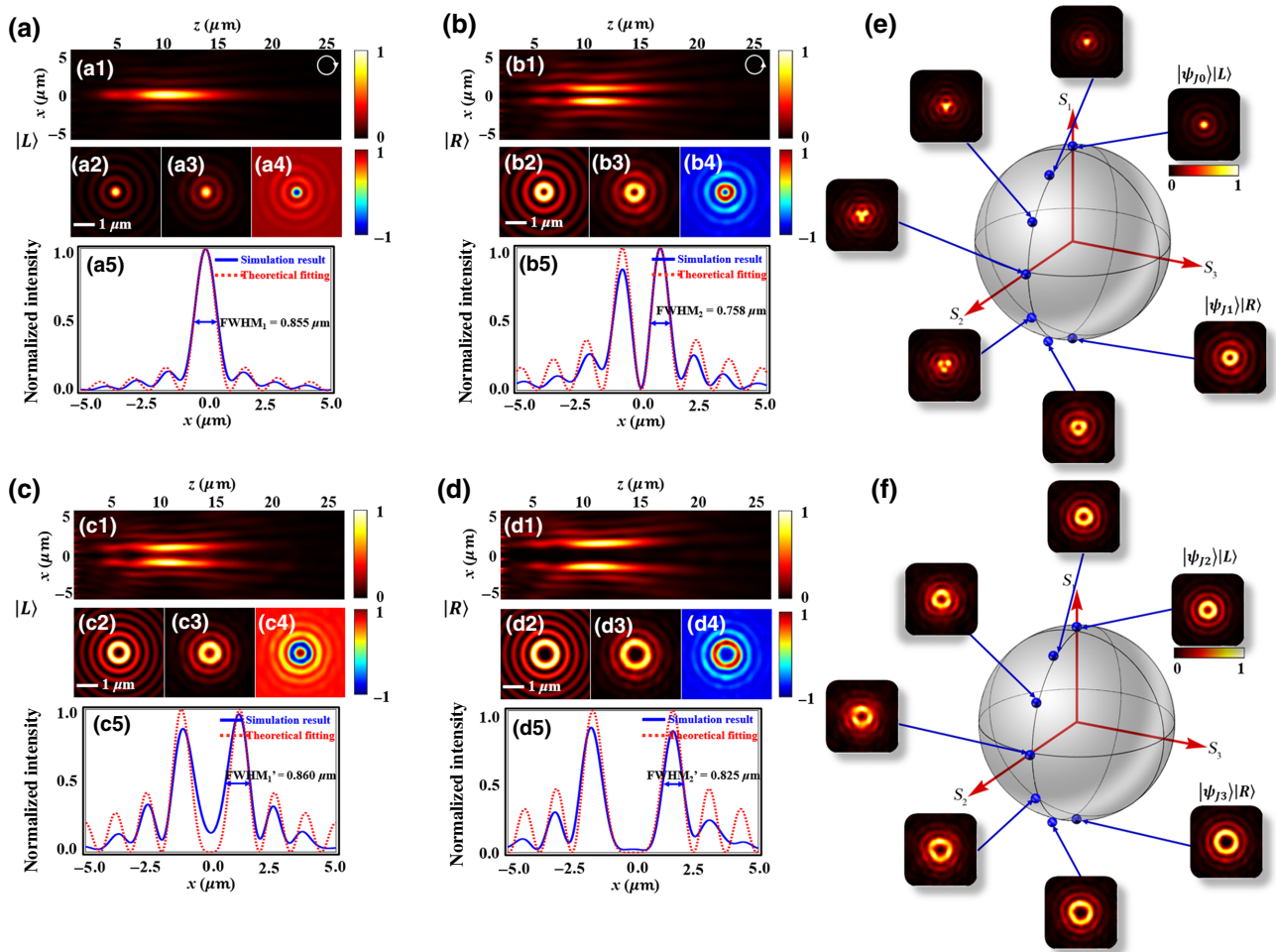
FIG. 2. Theoretical calculation and simulation results of Bessel beams with independent orders. (a),(b) Simulated longitudinal intensity distributions (a1),(b1), calculated (a2),(b2) and simulated (a3),(b3) transverse intensity distributions, Stokes parameters S_3 (a4), and normalized intensity profiles (a5),(b5) with efficiencies of 61.53% and 61.40% for case 1. (c),(d) Simulated longitudinal intensity distributions (c1),(d1), calculated (c2),(d2) and simulated (c3,d3) intensity of transverse patterns, Stokes parameters S_3 (c4),(d4), and normalized intensity profiles (c5),(d5) with efficiencies of 60.02% and 57.84% for case 2. (e),(f) Snapshots of transverse patterns for different incident polarizations on path of the hybrid-order Poincaré sphere.

of singularity in both cases split into three parts from the center and gradually extend outward to three parts. To explain this intriguing phenomenon, the helical phase and the phase of the axicon carried by the high-NA Bessel beam have to be taken into account simultaneously. The generation of a Bessel beam is associated with the tight-focusing effect, which leads to the conversion from SAM to OAM. For tight focusing, the spin-to-orbit conversion leads to the following relation [30]:

$$|L\rangle \rightarrow e^{i(n-2)\phi}|L\rangle + e^{in\phi}|R\rangle + e^{i(n-1)\phi}|z\rangle,$$

$$|R\rangle \rightarrow e^{i(n+3)\phi}|R\rangle + e^{i(n+1)\phi}|L\rangle + e^{i(n+2)\phi}|z\rangle, \quad (6)$$

where $|L\rangle$, $|R\rangle$, and $|z\rangle$ represent the LCP, RCP, and longitudinal components, respectively. Due to the presence of

the geometric phase, only the cross polarization of the output field needs be considered [i.e., $e^{in\phi}|R\rangle \gg e^{i(n-2)\phi}|L\rangle$, $e^{i(n+1)\phi}|L\rangle \gg e^{i(n+3)\phi}|R\rangle$]. Moreover, compared with the J plate, the longitudinal component has the same magnitude and the interference is most significant for the linearly polarized (LP) state incidence. In this context, both the dynamic and geometric phases manipulate the helical phase, which is determined by the spin-orbit interactions of light, whereas tight focusing caused by the phase of the axicon is determined only by the geometric phase. Figures 3(a) and 3(b) give theoretical and simulation results of the longitudinal component at the LCP, LP, and RCP incidences. Additionally, this physical mechanism also appears in the focused-field-carrying OAM [39].

To further estimate the electric field distribution, the polarization state of the input field on the hybrid-order PS is divided into LCP and RCP components. Therefore,
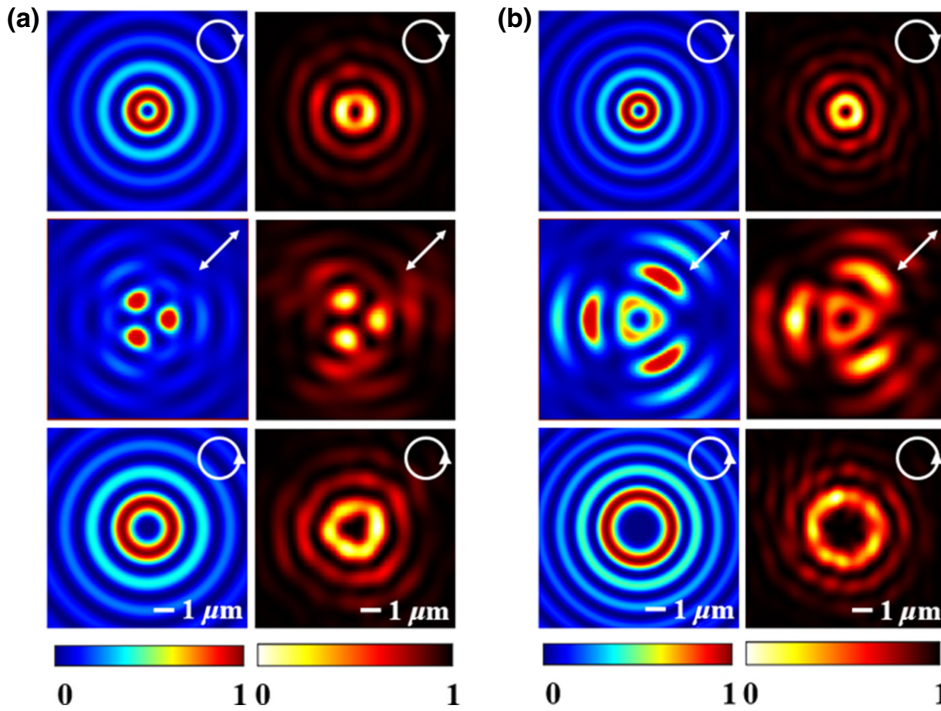
FIG. 3. Theoretical calculation (left) and simulation results (right) of longitudinal component of Bessel beam with independent orders for LCP, LP, and RCP incidence. (a) Orders $n_1 = 0$, $n_2 = 1$ for case 1. (b) Orders $n_1' = 0$, $n_2' = 1$ for case 2.

by illuminating any CP state of different polarization angles, the electric field can be expressed by RCP and LCP as $[(1 + i\mu)/(\sqrt{2}\sqrt{1 + |\mu|^2})]e^{i\varphi^+}|R\rangle$ and $[(1 - i\mu)/(\sqrt{2}\sqrt{1 + |\mu|^2})]e^{i\varphi^-}|L\rangle$ [where $\mu = exp(i\delta)$]. Then, the

total output field can also be divided into cross-orthogonal CP states. By using the Fresnel diffraction integral, the distribution of the electric field related to the polarization angle can be written as

$$\psi = \frac{2\pi \exp(ik_z)}{i\sqrt{\lambda z}} \left[\frac{1+i\mu}{\sqrt{2}\sqrt{1 + |\mu|^2}} e^{in\phi} J_n(k_r\text{NA}) + \frac{1 - i\mu}{\sqrt{2}\sqrt{1 + |\mu|^2}} e^{i(n+1)\phi} J_{n+1}(k_r\text{NA}) \right]. \quad (7)$$

As a result, by varying the polarization angle of the incident light, the electric field generated by the metasurface can be tuned continuously and estimated by Eq. (7).

IV. BESSEL BEAM WITH DIFFERENT NAS

As another parameter to control the properties of a Bessel beam, different NAs change the size of the main lobe of the Bessel spot. Thus, the results for a zero-order Bessel beam based on two samples with the same radius, $R = 20$ μm, and $\text{NA}_1 = 0.4$ and $\text{NA}_2 = 0.6$ for case 3, and $\text{NA}_1' = 0.6$ and $\text{NA}_2' = 0.8$ for case 4, at orthogonal CP state incidence are shown in Fig. 4. One can see from Figs. 4(a1)–4(d1) that the NA affects the effective depth of the Bessel beam along the propagation direction. The longitudinal intensity distributions; calculated and simulated transverse intensity distributions, with

FWHM$_1 \sim 0.890$ μm, FWHM$_2 \sim 0.886$ μm, FWHM$_1' \sim 0.889$ μm, and FWHM$_2' \sim 0.841$ μm; and Stokes parameters S_3 at $z = 11$ μm, $z = 7$ μm for case 3 and $z = 7$ μm, $z = 3.5$ μm for case 4 are shown in Figs. 4(a)–4(d). The efficiencies of the Bessel beams for LCP and RCP incidence are calculated to be 66.58%, 64.36% and 64.82%, 57.04%, respectively. As the incident polarization angle changes, the main lobe shrinks, increasing the number of side lobes, and the hybrid-order PS reduces to the standard plane-wave PS, as shown in Figs. 4(e) and 4(f). It can be found that the symmetry of the spot is broken for the incident elliptically polarized state, which can be explained by the interference of longitudinal components due to the tight-focusing effect [30]. On the basis of the previous discussion, the results with LCP, LP, and RCP incidence are shown in Fig. 5, indicating that theoretical calculations are in agreement with the simulation. Similarly, to estimate the electric field with arbitrary incident polarization, by
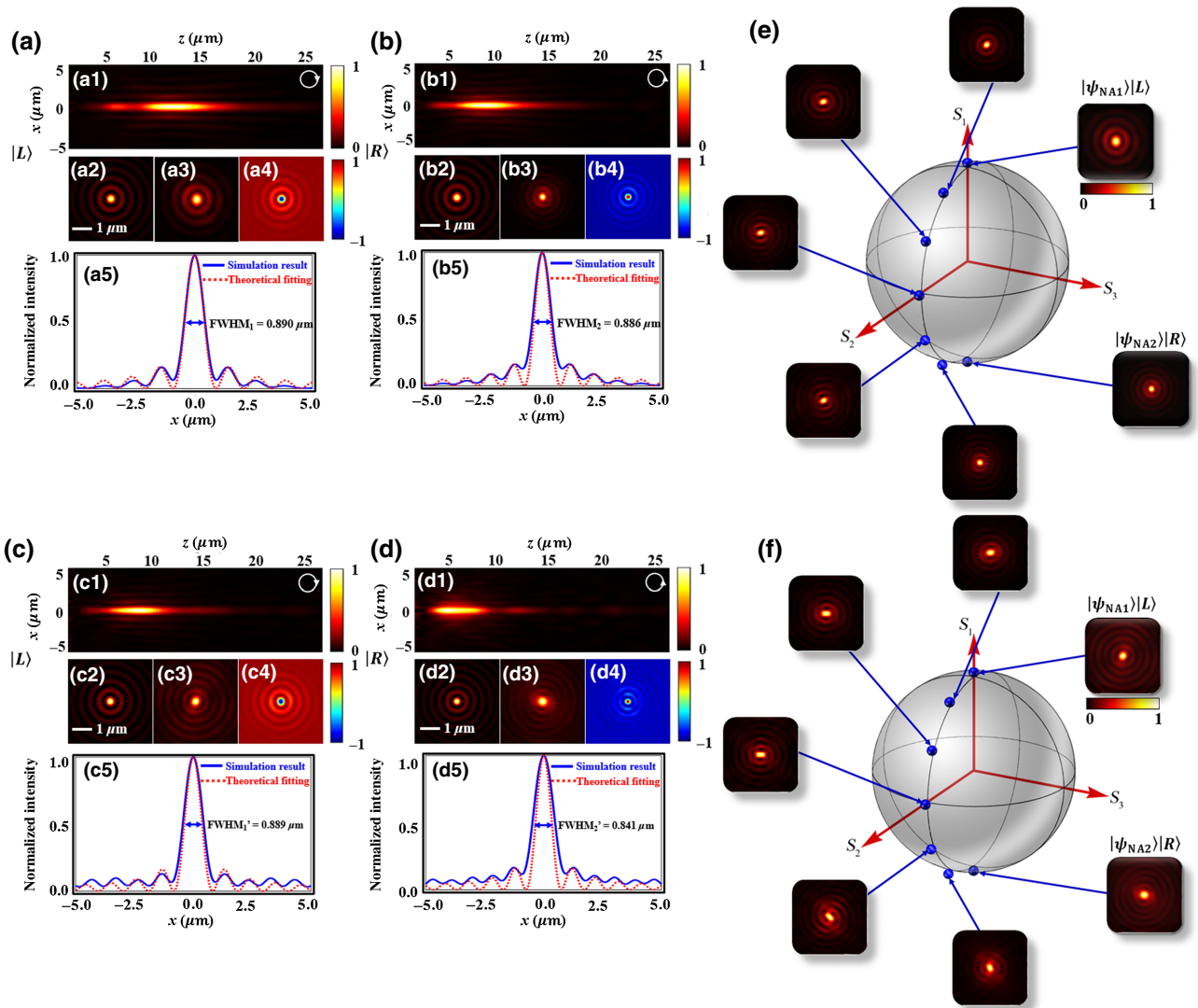
FIG. 4.   Theoretical calculation and simulation results of Bessel beams with different NAs. (a),(b) Simulated longitudinal intensity distributions (a1),(b1), calculated (a2),(b2) and simulated (a3),(b3) transverse intensity distributions, Stokes parameters S_3 (a4),(b4), and normalized intensity profiles (a5),(b5) for case 3 with efficiencies of 66.58% and 64.36%. (c),(d) Longitudinal intensity distributions (c1),(d1), calculated (c2),(d2) and simulated (c3),(d3) transverse intensity distributions, Stokes parameters S_3 (c4),(d4), and normalized intensity profiles (c5),(d5) for case 4 with efficiencies of 64.82% and 57.04%. (e),(f) Snapshots of transverse patterns for different incident polarizations on path of the standard plane-wave Poincaré sphere.

$$\psi' = \frac{2\pi \exp(ik_z)}{i\sqrt{\lambda z}} \left[\frac{1+i\mu}{\sqrt{2}\sqrt{1+|\mu|^2}} J_0(k_r \mathrm{NA}_1) + \frac{1-i\mu}{\sqrt{2}\sqrt{1+|\mu|^2}} J_0(k_r \mathrm{NA}_2) \right]. \tag{8}$$

Consequently, by changing the polarization angle of incident light, the main lobe of Bessel beams with different sizes can be tailored.

V. DUAL-BESSEL BEAM GENERATION

Furthermore, to develop the potential capability of spin-multiplexing functions, the photonic spin Hall effect

[35,37] can be used to simultaneously generate symmetric and asymmetric dual-Bessel beams with different deflection directions and orders at the LP state incidence, by introducing the offset values Δx_1 and Δx_2 into Eq. (5), which indicates that the conjugated properties of Bessel beams with different incident polarizations can be broken. Here, we demonstrate the symmetric dual-Bessel beams of the same ($n_1 = n_2 = 0$) and different orders ($n_1 = 0$, $n_2 = 1$)
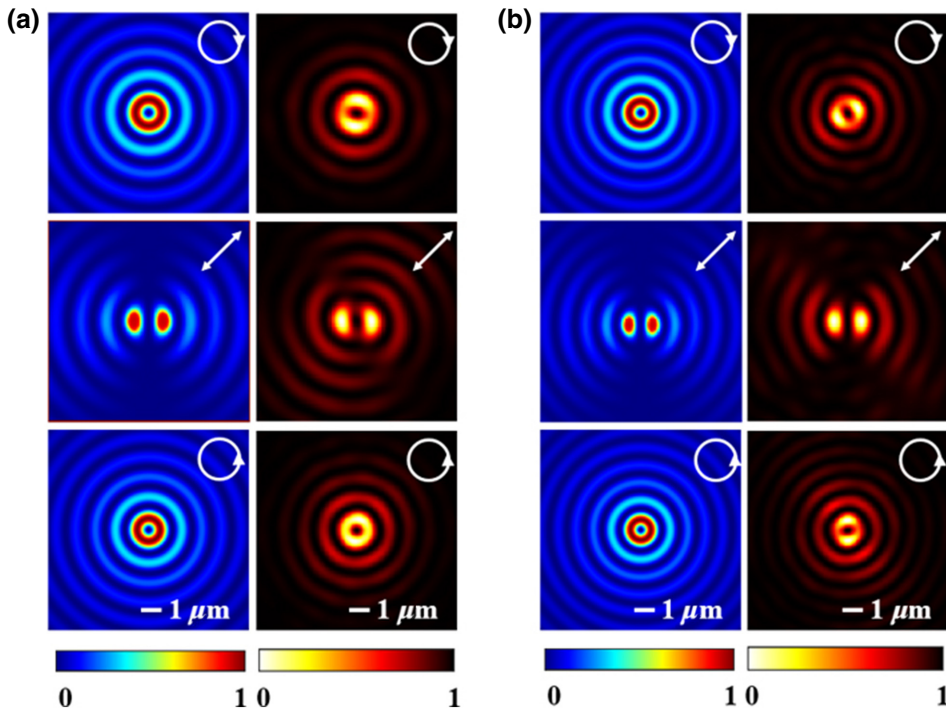
FIG. 5. Theoretical (left) and simulation (right) results of longitudinal component of Bessel beams with different NAs for LCP, LP, and RCP incidence. (a) $NA_1 = 0.4$, $NA_2 = 0.6$ for case 3. (b) $NA_1' = 0.6$, $NA_2' = 0.8$ for case 4.

with deflection distances of $\Delta x_1 = -3.5\,\mu m$ and $\Delta x_2 = 3.5\,\mu m$, as shown in Figs. 6(a) and 6(c), while the asymmetric situation with $\Delta x_1 = -4\,\mu m$ and $\Delta x_2 = 2.5\,\mu m$ is shown in Figs. 6(c) and 6(d).

VI. CONCLUSION

We investigate the generation and conversion dynamics of typical nondiffracting beams with a photonic spin-dependent metasurface, which can flexibly and effectively control and manipulate the output beams by varying the incident polarization of light. Singular splitting of the independent Bessel beams during conversion is due to the contribution of the longitudinal component caused by the tight-focusing effect, which is proved by both theoretical and simulation results. The proposed model of the electric field at arbitrary incident polarization is estimated by decomposing the orthogonal CP polarized states and applying the Fresnel diffraction integral. Finally, simulated dual-Bessel beams with symmetric and asymmetric splitting are also demonstrated. With the development of micro- and nanofabrication technology, we envision this method to be utilized in miniature optical platform exploitation, where different structured beams of high NA
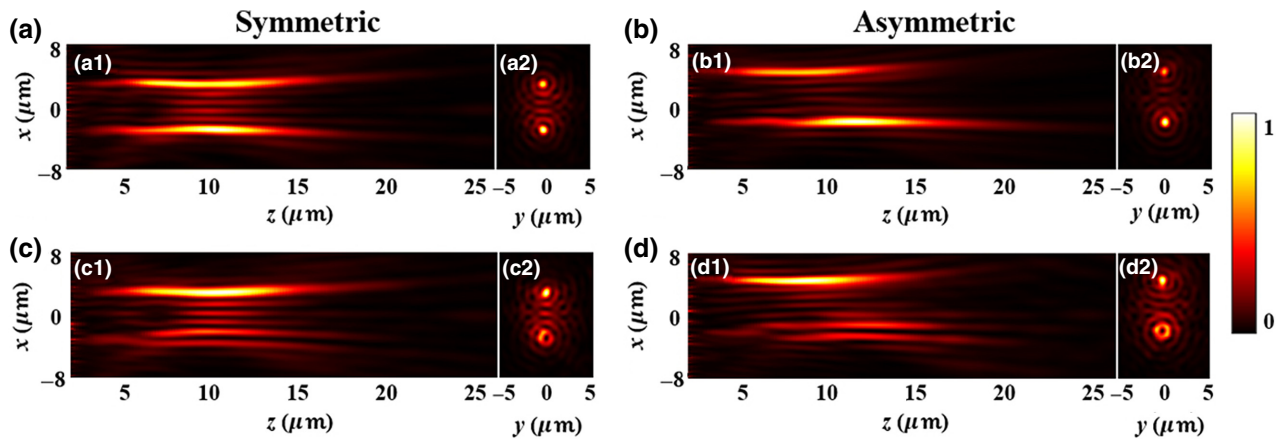

FIG. 6. Longitudinal and transverse intensity distributions of dual-Bessel beams. (a),(b) Same order ($n_1 = n_2 = 0$) with symmetric (a1),(a2) and asymmetric splitting (b1),(b2). (c),(d) Different order ($n_1 = 0$, $n_2 = 1$) with symmetric (c1),(c2) and asymmetric splitting (d1),(d2).

are required and can be applied in the fields of astrophotonics, switchable superresolution microscopy, and optical manipulation of microparticles.

[1] J. Durnin, Exact solutions for nondiffracting beams I the scalar theory, J. Opt. Soc. Am. A **4**, 651 (1987).

[2] C. Sheng, R. Bekenstein, H. Liu, S. Zhu, and M. Segev, Wavefront shaping through emulated curved space in waveguide settings, Nat. Commun. **7**, 10747 (2016).

[3] T. A. Planchon, L. Gao, D. E. Milkie, M. W. Davidson, J. A. Galbraith, C. G. Galbraith, and E. Betzig, Rapid three-dimensional isotropic imaging of living cells using bessel beam plane illumination, Nat. Methods **8**, 417 (2011).

[4] H. Jia, X. Yu, Y. Yang, X. Zhou, S. Yan, C. Liu, M. Lei, and B. Yao, Axial resolution enhancement of light-sheet microscopy by double scanning of bessel beam and its complementary beam, J. Biophotonics **12**, e201800094 (2019).

[5] L. Gao, L. Shao, B. Chen, and E. Betzig, 3D live fluorescence imaging of cellular dynamics using bessel beam plane illumination microscopy, Nat. Photonics **9**, 1083 (2014).

[6] J. Chen, J. Ng, Z. Lin, and C. T. Chan, Optical pulling force, Nat. Photonics **5**, 531 (2011).

[7] A. Dogariu, S. Sukhov, and J. Sáenz, Optically induced 'negative forces', Nat. Photonics **7**, 24 (2013).

[8] D. Debeer, S. R. Hartmann, and R. Friedberg, Comment on "Diffraction-Free Beams", Phys. Rev. Lett. **59**, 2611 (1987).

[9] S. Monk, J. Arlt, D. A. Robertson, J. Courtial, and M. J. Padgett, The generation of Bessel beams at millimetre-wave frequencies by use of an axicon, Opt. Commun. **170**, 213 (1999).

[10] J. Turunen, A. Vasara, and A. T. Friberg, Holographic generation of diffraction-free beams, Appl. Opt. **27**, 3959 (1988).

[11] F. Monti Di Sopra, H. P. Gauggel, M. Brunner, R. Hövel, M. Moser, and H. P. Zappe, Long-term spectral stability of singlemode VCSELs, Electron. Lett. **37**, 832 (2001).

[12] W. T. Chen, M. Khorasaninejad, A. Y. Zhu, J. Oh, R. C. Devlin, A. Zaidi, and F. Capasso, Generation of wavelength-independent subwavelength bessel beams using metasurfaces, Light Sci. Appl. **6**, e16259 (2017).

[13] K. Huang, F. Qin, H. Liu, H. Ye, C. Qiu, M. Hong, B. Luk'Yanchuk, and J. Teng, Planar diffractive lenses:

Fundamentals, functionalities, and applications, Adv. Mater. **30**, 1704556 (2018).

[14] N. Yu, P. Genevet, M. A. Kats, F. Aieta, J. P. Tetienne, F. Capasso, and Z. Gaburro, Light propagation with phase discontinuities: Generalized laws of reflection and refraction, Science **334**, 333 (2011).

[15] X. Chen, L. Huang, H. Mühlenbernd, G. Li, B. Bai, Q. Tan, G. Jin, C. Qiu, S. Zhang, and T. Zentgraf, Dual-polarity plasmonic metalens for visible light, Nat. Commun. **3**, 1198 (2012).

[16] L. Huang, X. Chen, H. Mühlenbernd, G. Li, B. Bai, Q. Tan, G. Jin, T. Zentgraf, and S. Zhang, Dispersionless phase discontinuities for controlling light propagation, Nano Lett. **12**, 5750 (2012).

[17] A. Arbabi, Y. Horie, M. Bagheri, and A. Faraon, Dielectric metasurfaces for complete control of phase and polarization with subwavelength spatial resolution and high transmission, Nat. Nanotechnol. **10**, 937 (2015).

[18] M. Khorasaninejad, W. T. Chen, R. Declin, J. oh, A. Y. Zhu, and F. Capasso, Metalenses at visible wavelengths: Diffraction-limited focusing and subwavelength resolution imaging, Science **352**, 1190 (2016).

[19] S. Wang, P. C. Wu, V. C. Su, Y. C. Lai, C. H. Chu, J. W. Chen, S. H. Lu, J. Chen, B. Xu, C. H. Kuan, T. Li, S. Zhu, and D. P. Tsai, Broadband achromatic optical metasurface devices, Nat. Commun. **8**, 187 (2017).

[20] S. Wang, P. C. Wu, V. Su, Y. Lai, M. Chen, H. Y. Kuo, B. H. Chen, Y. H. Chen, T. Huang, J. Wang, R. Lin, C. Kuan, T. Li, Z. Wang, S. Zhu, and D. P. Tsai, A broadband achromatic metalens in the visible, Nat. Nanotechnol. **13**, 227 (2018).

[21] W. T. Chen, A. Y. Zhu, V. Sanjeev, M. Khorasaninejad, Z. Shi, E. Lee, and F. Capasso, A broadband achromatic metalens for focusing and imaging in the visible, Nat. Nanotechnol. **13**, 220 (2018).

[22] R. J. Lin, V. Su, S. Wang, M. K. Chen, T. L. Chung, Y. H. Chen, H. Y. Kuo, J. Chen, J. Chen, Y. Huang, J. Wang, C. H. Chu, P. C. Wu, T. Li, Z. Wang, S. Zhu, and D. P. Tsai, Achromatic metalens array for full-colour light-field imaging, Nat. Nanotechnol. **14**, 227 (2019).

[23] L. Li, Z. Liu, X. Ren, S. Wang, V. Su, M. Chen, C. H. Chu, H. Y. Kuo, B. Liu, W. Zang, G. Guo, L. Zhang, Z. Wang, S. Zhu, and D. P. Tsai, Metalens-array–based high-dimensional and multiphoton quantum source, Science **368**, 1487 (2020).

[24] K. Huang, H. Ye, J. Teng, S. P. Yeo, B. Luk'Yanchuk, and C. Qiu, Optimization-free superoscillatory lens using phase and amplitude masks, Laser Photonics Rev. **8**, 152 (2014).

[25] H. Li, Y. Cao, L. Zhou, X. Xu, T. Zhu, Y. Shi, C.-W. Qiu, and W. Ding, Optical pulling forces and their applications, Adv. Opt. Photonics **12**, 288 (2020).

[26] C. Pfeiffer and A. Grbic, Generating stable tractor beams with dielectric metasurfaces, Phys. Rev. B **91**, 115408 (2015).

[27] Z. Wang, S. Dong, W. Luo, M. Jia, Z. Liang, Q. He, S. Sun, and L. Zhou, High-efficiency generation of bessel beams with transmissive metasurfaces, Appl. Phys. Lett. **112**, 191901 (2018).

[28] M. R. Akram, M. Q. Mehmood, T. Tauqeer, A. S. Rana, I. D. Rukhlenko, and W. Zhu, Highly efficient generation

of bessel beams with polarization insensitive metasurfaces, Opt. Express **27,** 9467 (2019).

[29] K. Y. Bliokh, F. J. Rodríguez-Fortuño, F. Nori, and A. V. Zayats, Spin-orbit interactions of light, Nat. Photonics **9,** 796 (2015).

[30] S. Yan, M. Li, Y. Liang, Y. Cai, and B. Yao, Spin momentum-dependent orbital motion, New J. Phys. **22,** 053009 (2020).

[31] R. C. Devlin, A. Ambrosio, N. A. Rubin, J. P. B. Mueller, and F. Capasso, Arbitrary spin-to–orbital angular momentum conversion of light, Science **358,** 896 (2017).

[32] X. Xu and M. Nieto-Vesperinas, Azimuthal Imaginary Poynting Momentum Density, Phys. Rev. Lett. **123,** 233902 (2019).

[33] X. Xu, M. Nieto-Vesperinas, C.-W. Qiu, X. Liu, D. Gao, Y. Zhang, and B. Li, Kerker-Type intensity-gradient force of light, Laser Photon. Rev. **14,** 1900265 (2020).

[34] J. P. Balthasar Mueller, N. A. Rubin, R. C. Devlin, B. Groever, and F. Capasso, Metasurface Polarization Optics: Independent Phase Control of Arbitrary Orthogonal States of Polarization, Phys. Rev. Lett. **118,** 113901 (2017).

[35] S. Li, X. Li, G. Wang, S. Liu, L. Zhang, C. Zeng, L. Wang, Q. Sun, W. Zhao, and W. Zhang, Multidimensional manipulation of photonic spin hall effect with a single-layer dielectric metasurface, Adv. Optical Mater. **7,** 1801365 (2018).

[36] J. Zhang, L. Zhang, K. Huang, Z. Duan, and F. Zhao, Polarization-enabled tunable focusing by visible-light metalenses with geometric and propagation phase, J. Opt. **21,** 115102 (2019).

[37] R. Jin, L. Tang, J. Li, J. Wang, Q. Wang, Y. Liu, and Z. Dong, Experimental demonstration of multidimensional and multifunctional metalenses based on photonic spin hall effect, ACS Photonics **7,** 512 (2020).

[38] X. N. Yi, Y. C. Liu, X. H. Ling, X. X. Zhou, Y. G. Ke, H. L. Luo, S. C. Wen, and D. Y. Fan, Hybrid-order poincaré sphere, Phys. Rev. A. **91,** 023801 (2015).

[39] See the Supplemental Material at http://link.aps.org/supplemental/10.1103/PhysRevApplied.15.014059 for a comparison between the focused field carrying OAM and the higher-order Bessel beam, as well as simulation results with independent NAs in conversion processes.